

Raman spectroscopy of rare-earth orthoferrites $R\text{FeO}_3$ ($R = \text{La}, \text{Sm}, \text{Eu}, \text{Gd}, \text{Tb}, \text{Dy}$)

Mads Christof Weber,^{1,2} Mael Guennou,¹ Hong Jian Zhao,¹ Jorge Íñiguez,¹ Rui Vilarinho,³ Abílio Almeida,³ Joaquim Agostinho Moreira,³ and Jens Kreisel^{1,2}

¹*Materials Research and Technology Department,*

Luxembourg Institute of Science and Technology, 41 rue du Brill, L-4422 Belvaux, Luxembourg

²*Physics and Materials Science Research Unit, University of Luxembourg, 41 Rue du Brill, L-4422 Belvaux, Luxembourg*

³*IFIMUP and IN-Institute of Nanoscience and Nanotechnology,*

Physics and Astronomy Department of Faculty of Sciences of University of Porto, Porto, Portugal

(Dated: September 27, 2016)

We report a Raman scattering study of six rare earth orthoferrites $R\text{FeO}_3$, with $R = \text{La}, \text{Sm}, \text{Eu}, \text{Gd}, \text{Tb}, \text{Dy}$. The use of extensive polarized Raman scattering of SmFeO_3 and first-principles calculations enable the assignment of the observed phonon modes to vibrational symmetries and atomic displacements. The assignment of the spectra and their comparison throughout the whole series allows correlating the phonon modes with the orthorhombic structural distortions of $R\text{FeO}_3$ perovskites. In particular, the positions of two specific A_g modes scale linearly with the two FeO_6 octahedra tilt angles, allowing the distortion throughout the series. At variance with literature, we find that the two octahedra tilt angles scale differently with the vibration frequencies of their respective A_g modes. This behavior as well as the general relations between the tilt angles, the frequencies of the associated modes and the ionic radii are rationalized in a simple Landau model. The reported Raman spectra and associated phonon-mode assignment provide reference data for structural investigations of the whole series of orthoferrites.

Keywords: Orthoferrites, Raman spectroscopy, LaFeO_3 , SmFeO_3 , GdFeO_3 , EuFeO_3 , TbFeO_3

I. INTRODUCTION

In the past, $R\text{FeO}_3$ perovskites have attracted considerable interest due to their remarkable magnetic properties [1–3]. At ambient conditions, they adopt an orthorhombic $Pnma$ structure, hence their common name orthoferrites. This orthorhombic structure can be derived from the ideal cubic perovskite structure by rotations (tilts) of its FeO_6 octahedra, where the tilt angles can be tuned by the size of the rare earth R . All members of the family possess a canted antiferromagnetic structure arising from spin moments of the Fe^{3+} cations. The antiferromagnetic ordering of the iron ions occurs at a Néel temperature T_N around 650 to 700 K. Several orthoferrites show a spin reorientation at lower temperatures. In contrast to the Fe^{3+} cations, the magnetic moments of the R^{3+} rare earth ions order below 10 K. Interestingly, a so-called compensation point where moments of the two sublattices cancel has been reported for several $R\text{FeO}_3$ compounds [1]. More recent studies have also focused on spin-ordering processes of the rare earth ions [4–6] and the interaction between magnetism and crystal lattice, including the role of spin-lattice coupling in multiferroic properties [7–11].

Tilts of the FeO_6 -octahedra are the main structural parameters to tune the band overlap and thus the physical properties of orthoferrites. Unfortunately, tilt angles are chronically difficult to probe directly, specifically in thin films, because they require in depth diffraction experiments needing at best large-scale instruments using neutron or synchrotron radiation. Alternatively, Raman spectroscopy (RS) is a well-known technique to follow tilt-driven soft mode phase transitions [12–14]. More re-

cently, it has been shown that RS is also an appropriate probe for the investigation of lattice distortions and slight changes in octahedra rotations [15–18]. Further to this, RS is an ideal probe for the investigation of spin-phonon coupling phenomena [19–23]. Finally, RS is a now widely used technique for probing even subtle strain-induced structural modifications in oxide thin films [24–26]. All such investigations rely on thorough reference spectra, solid knowledge of the relations between structural distortions phonon modes, and on a proper band assignment of vibrational bands in terms of symmetry and atomic displacement patterns. The present paper aims at providing this fundamental knowledge by investigating both experimentally and theoretically a series of orthoferrites and by proposing a consolidated view of this new data together with available literature data on other members of the family.

II. EXPERIMENTAL

SmFeO_3 single crystals were grown in an optical-floating-zone furnace as described elsewhere [5]. Three single domain platelets were oriented along the three orthorhombic directions, with their edges also parallel to crystallographic axes, and polished down to a thickness of 100 μm . The single domain state was verified by XRD and polarized light microscopy. A SmFeO_3 crystal was manually grinded to acquire a homogeneous powder. LaFeO_3 and EuFeO_3 powders were obtained by conventional solid state reactions. GdFeO_3 and DyFeO_3 powder samples were prepared using the urea sol-gel combustion method, reported elsewhere [27] and their quality was checked by XRD and SEM. TbFeO_3 samples

were prepared by floating zone method in FZ-T-4000 (Crystal Systems Corporation) mirror furnace. As starting materials, Fe_2O_3 (purity 2N, supplier: Sigma Aldrich), and Tb_4O_7 (purity 3N, supplier: Alpha Aesar) were used. They were mixed in a Tb:Fe stoichiometric ratio, cold pressed into rods and sintered at 1100 °C from 12 to 14 hours in air. Their quality was checked by X-ray powder diffraction and by energy dispersion X-ray analysis, confirming the single perovskite phase.

Raman scattering measurements were performed with an inVia Renishaw Reflex Raman Microscope in micro-Raman mode. For excitation a 633 nm He-Ne laser with a spectral cut-off at 70 cm^{-1} was used. Great care was taken to avoid heating of the sample by limiting the incident laser power. Samples were cooled to liquid nitrogen temperature in a Linkam THMS600 stage in order to reduce thermal broadening of the spectra and ease the identification of Raman bands. The band positions were obtained by fitting the spectra with Lorentzian functions.

For the calculations we used density functional theory (DFT) within the generalized gradient approximation revised for solids,[28] as implemented in the Vienna ab-initio Simulation Package (VASP)[29, 30]. For a better treatment of iron's 3d electrons, we used the Hubbard-like correction proposed by Dudarev *et al.*,[31] with $U_{\text{eff}} = 4$ eV. The ionic cores were treated within the projection augmented approximation (PAW),[32] and the following electrons were explicitly solved in the simulations: O's $2s^2 2p^4$; Fe's $3p^6 3d^7 4s^1$; $5p^6 5d^1 6s^2$ for Eu, Gd, Tb, and Dy; and $5s^2 5p^6 5d^1 6s^2$ for Sm and La. Note that, for the generation of the PAW potentials of the rare-earth species, a 3+ ionization state was assumed and the remaining 4f electrons were considered to be frozen in the ionic core. We explicitly checked in one case (GdFeO_3) that this approximation has a very small impact on the phonon frequencies and eigenvectors of interest in this work. Electronic wave functions are described in a basis of plane waves cut-off at 500 eV; reciprocal space integrals in the Brillouin zone of the 20-atom $Pnma$ cell were computed in a mesh of $4 \times 3 \times 5$ k -points. Structural optimization were performed until residual atomic forces are smaller than 0.01 eV/Å and phonon spectra were computed calculated by the finite difference method.

III. RESULTS AND DISCUSSION

A. Structural properties of the $R\text{FeO}_3$ series

Rare earth orthoferrites crystallize in an orthorhombic $Pnma$ structure at ambient conditions. With respect to the parent cubic perovskite phase $Pm\bar{3}m$, the $Pnma$ structure in orthoferrites can be derived by octahedral rotations. In Glazer's notation the octahedra tilt system is expressed as $a^-b^+a^-$ [33] or in pseudo-cubic settings as rotations θ , ϕ and Φ around the $[101]_{\text{pc}}$, $[010]_{\text{pc}}$

and $[111]_{\text{pc}}$, respectively [34]. Megaw has shown that it is sufficient to consider two independent angles θ and ϕ in order to describe the octahedral rotations of the $Pnma$ phase, assuming that the octahedral tilts a_x^- and a_z^- are approximately equal [35]. The angle Φ can be then expressed as $\cos \Phi = \cos \theta \cos \phi$ [34]. The octahedra rotations represent the order parameters for a hypothetical phase transition to the cubic $Pm\bar{3}m$ phase.

Similar to other perovskites with $Pnma$ structure, such as orthochromites $R\text{CrO}_3$, orthomanganites $R\text{MnO}_3$, orthonickelates $R\text{NiO}_3$, or orthoscandates $R\text{ScO}_3$, we can assume in good approximation that changing the rare earth affects negligibly the chemical bonding of the material. In contrast, the size of the rare earth impacts on the distortions of the structure, as measured for example by the tilt angles or the spontaneous strains, and can be continuously tuned by the size of the R^{3+} rare earth. The octahedral rotations are most reliably calculated from atomic positions following the formalism in Ref. 36. Table I summarizes the structural properties of all members of the $R\text{FeO}_3$ family. In Fig. 1 the structural evolution throughout the series is illustrated by the unit cell volume, which scales linearly with the ionic radius, and the lattice parameters.

The tolerance factor, given in Table I, is an indication for the stability of the perovskite structure. The closer its value is to 1, the closer the structure is to the cubic structure. From both, pseudo-cubic lattice parameters and tolerance factor, we find that with increasing ionic radius of the rare earth, from lutetium to lanthanum, the structure approaches a cubic metric. Notably, LaFeO_3 appears to be closest to a cubic structure.

B. Raman spectra and mode assignment

The orthorhombic $Pnma$ structure gives rise to 24 Raman-active vibrational modes [40], which decompose into $\Gamma_{\text{Raman}} = 7A_g + 5B_{1g} + 7B_{2g} + 5B_{3g}$. Schematically, the vibration modes below 200 cm^{-1} are mainly characterized by displacements of the heavy rare-earth ions. Above 300 cm^{-1} , motions of the light oxygen ions dominate, and in the intermediate frequency range vibration patterns involve both ions. Note that iron ions occupy centers of inversion in the $Pnma$ structure and, therefore, vibrations involving Fe^{3+} motions are not Raman-active. Fig. 2 shows the Raman spectra of six rare earth orthoferrites $R\text{FeO}_3$ ($R = \text{La}, \text{Sm}, \text{Eu}, \text{Gd}, \text{Tb}, \text{Dy}$), all measured at 80 K in order to reduce thermal broadening and make mode identification easier. Thanks to well-defined spectra, we identify between 18 and 21 vibration bands, depending on the compound. The remaining predicted modes are either masked by band overlap or their intensity is below the detection limit. The Raman spectra of SmFeO_3 , EuFeO_3 , GdFeO_3 , TbFeO_3 and DyFeO_3 present a similar overall shape which allows

Table I: Structural characteristics of $R\text{FeO}_3$ samples: R^{3+} ionic radii ($r_{R^{3+}}$ values given in an eightfold environment [37], lattice parameters, tolerance factor t calculated from the ionic radii following [34]: $t = (r_{R^{3+}} + r_{O^{2-}})/(\sqrt{2}(r_{Fe^{3+}} + r_{O^{2-}}))$ and octahedra tilt angles ($\phi[010]$, $\theta[101]$) calculated from the atomic coordinates. The data for the crystal structures are from Refs. [38, 39].

	Lattice parameters ($Pnma$ setting)						FeO ₆ octahedra tilt angle	
	$r_{R^{3+}}$	a (Å)	b (Å)	c (Å)	V (Å ³)	t	ϕ [010] (°)	θ [101] (°)
LaFeO ₃	1.160	5.563	7.867	5.553	243.022	0.934	7.3	12.2
PrFeO ₃	1.126	5.578	7.786	5.482	238.085	0.921	9.6	13.6
NdFeO ₃	1.109	5.584	7.768	5.453	236.532	0.915	10.0	14.5
SmFeO ₃	1.079	5.584	7.768	5.400	234.233	0.904	11.2	15.6
EuFeO ₃	1.066	5.606	7.685	5.372	231.437	0.899	11.6	16.0
GdFeO ₃	1.053	5.611	7.669	5.349	230.172	0.894	11.9	16.2
TbFeO ₃	1.040	5.602	7.623	5.326	227.442	0.889	12.1	16.9
DyFeO ₃	1.027	5.598	7.623	5.302	226.255	0.884	12.6	17.3
HoFeO ₃	1.015	5.598	7.602	5.278	224.611	0.880	12.7	17.7
ErFeO ₃	1.004	5.582	7.584	5.263	222.803	0.876	12.9	18.2
TmFeO ₃	0.994	5.576	7.584	5.251	222.056	0.872	12.9	18.6
YbFeO ₃	0.985	5.557	7.570	5.233	220.134	0.869	13.4	19.0
LuFeO ₃	0.977	5.547	7.565	5.213	218.753	0.866	13.2	19.5

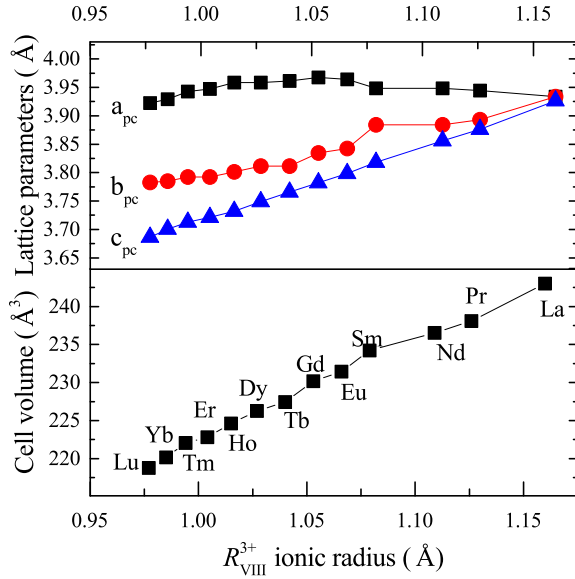


Figure 1: Variation of the pseudocubic cell parameters and orthorhombic unit-cell volume as a function of the R_{VIII}^{3+} ionic radius [37]. The lattice parameters are taken from ref.[38, 39].

to follow the evolution of particular bands throughout the series. The spectral signature of LaFeO_3 is distinctly different as explained by the size difference between La^{3+} and the closest Sm^{3+} and also its proximity to the cubic structure (see Fig. 1). This is similar to observations for other rare earth perovskites, where the Raman spec-

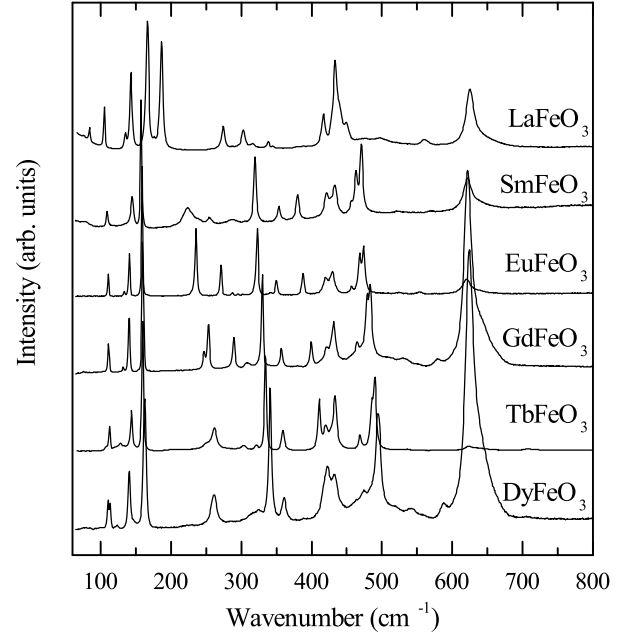


Figure 2: Raman spectra at 80 K of six rare earth orthoferrites $R\text{FeO}_3$ ($R = \text{La, Sm, Eu, Gd, Tb, Dy}$) collected with a 633 nm He-Ne laser line.

trum of the lanthanum member is systematically different when compared to the remaining members of the series [15, 17, 41]. This will be elaborated on later in the discussion.

In order to go further in the mode assignment, we

performed a polarized Raman study of SmFeO_3 single crystals. Indeed, the identification of the symmetry of the difference Raman bands is difficult if not impossible from powder samples alone. On the other hand, polarized Raman spectroscopy on well-oriented single crystals allows identifying the symmetries of phonon bands. Raman modes of a given symmetry can be selectively probed through particular configurations of incident and scattered light polarizations with respect to the orientation of the crystal. This experimental configuration is expressed in Porto's notation [42]. In the following, we use X, Y, Z to indicate the crystallographic axes in the $Pnma$ setting. Figure 3 presents the obtained results for SmFeO_3 single crystals for twelve scattering configurations. Fig. 3a shows the Raman spectra for A_g configurations modes, while spectra exhibiting B_{1g} , B_{2g} or B_{3g} modes are given in Fig. 3b. In total, we identify all expected A_g , six B_{2g} modes and four out of five B_{1g} and B_{3g} modes (see Table II).

In a next step, we run DFT calculations of phonon modes for all measured orthoferrites in order to confirm the mode symmetries and associate a vibrational pattern to each mode. A summary of all theoretical and experimental band frequencies with their symmetry and characteristic atomic motions is given in Table II. The calculated frequencies are in very good agreement with our experimental values and the continuous evolution of the spectral signature.

The band between 600 and 650 cm^{-1} in Fig. 3a shows a peculiar behaviour and needs a specific discussion. First, as can be seen in Fig. 2, its frequency seems to be independent of the rare earth. Besides, it shows intensity variations from sample to sample that contrast with the other bands, and also exhibits a strong asymmetry. For SmFeO_3 , Fig. 3 shows that these bands appear with very low intensity in crossed polarization but are strongly visible in parallel configuration, which would rather point to a A_g symmetry. However, as can be seen in Table II, the calculations predict two bands of B_{2g} and B_{3g} symmetry in this region, but no A_g Raman mode, and all A_g modes are already conclusively attributed. We therefore conclude that this band is not a first-order Raman mode.

A precise interpretation for this band is beyond the scope of this work, but we note that similar features have been described for other perovskite oxides, with unclear assignments and conflicting reports. As an example, Iliev et al. discussed it for LaCrO_3 [43] and demonstrated that its intensity can be reduced by annealing the sample in vacuum. Therefore it seems likely that it is related to chemical defects of the lattice [43]. Here, we note that DyFeO_3 and GdFeO_3 , where this band is stronger, were produced by a chemical metalorganic process, whereas the other samples (LaFeO_3 , SmFeO_3 , EuFeO_3 and TbFeO_3) were synthesized by solid-state reaction. A difference in defect chemistry originating from different growth processes is therefore plausible.

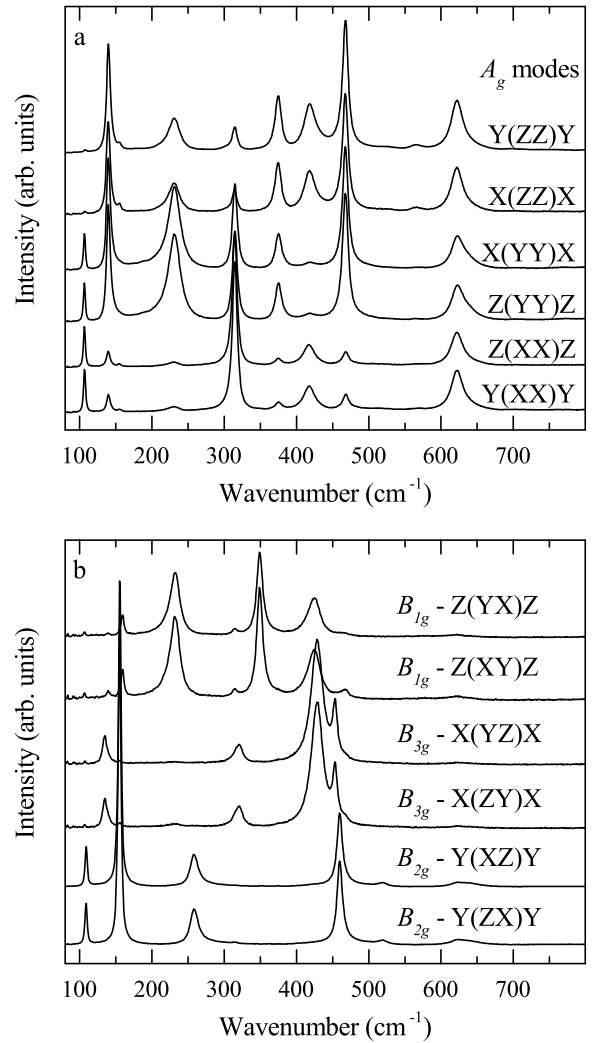


Figure 3: Polarized Raman spectra of SmFeO_3 at ambient conditions. The measurement configurations are given in Porto's notation, in a) for the vibration modes of A_g symmetry and in b) for the vibration modes of B_{1g} , B_{2g} and B_{3g} symmetries. X, Y and Z correspond to the orthorhombic axes in the $Pnma$ space group.

C. Phonon Raman modes vs. ionic radii and octahedra tilt angle

Figure 4 presents the evolution of the band positions for the different orthoferrites as a function of the ionic radii of the rare earths. Overall, Raman bands shift to lower frequencies with increasing $r_{R^{3+}}$, which naturally correlates with the increase in volume and, therefore, of most bond lengths. It can be seen that the frequencies of the Raman modes are differently sensitive to the change of rare earth. This is understood in the context of the structural instabilities in the $Pnma$ structure. In the framework of Landau theory, the two octahedra rotations represent the two order parameters for a phase

Table II: Experimental and theoretical band positions, the corresponding symmetry assignment and main atomic motions of the observed Raman modes in $R\text{FeO}_3$. The main atomic motions are extracted from DFT calculations. Refer to the supplemental materials for the displacements of all ions.

Symmetry	LaFeO ₃		SmFeO ₃		EuFeO ₃		GdFeO ₃		TbFeO ₃		DyFeO ₃		main atomic motion
	80 K	calc.	80 K	calc.	80 K	calc.	80 K	calc.	80 K	calc.	80 K	calc.	
$A_g(1)$	84.5	89	109.5	109	110.9	112	111.1	111	112.5	112	113.3	112	$R(x)$, in-phase in x-z, out-of-phase in y
$A_g(2)$	135.3	127	144.2	138	140.7	140	140.4	137	143.9	136	140.5	135	$R(z)$, out-of-phase
$A_g(3)$	186.6	183	223.9	244	235.1	252	253.2	255	261.9	259	261.5	262	$[010]_{\text{pc}}$ FeO ₆ rotation, in-phase
$A_g(4)$	274.2	273	319.1	320	323.2	325	329.9	330	334.5	330	341.1	332	O(1) x-z plane
$A_g(5)$	302.8	306	379.5	383	387.8	397	399.4	405	410.9	410	422.4	422	$[101]_{\text{pc}}$ FeO ₆ rotation, in-phase
$A_g(6)$	449.8	433	420.7	413	419.6	414	420.9	416	420.1	416	417.3	415	Fe-O(2) stretching, in-phase
$A_g(7)$	433.3	413	470.7	468	474.0	476	483.6	480	490.1	484	496.8	490	O(1)-Fe-O(2) scissor-like bending
$B_{1g}(1)$		169	160.7	151		149		143		139		135	$R(y)$ in-phase in x-z, out-of-phase in y
$B_{1g}(2)$		148	238.7	233	236.4	243	247.1	244	251.9	248		250	$[010]_{\text{pc}}$ FeO ₆ rotation, out-of-phase
$B_{1g}(3)$	338.1	328	353.3	352	350.0	356	357.0	356	359.2	356	360.9	359	$[010]_{\text{pc}}$ FeO ₆ rotating, out-of-phase
$B_{1g}(4)$	442.3	425	426.4	422	425.8	424	428.8	426	427.7	425	427.4	427	Fe-O(2) stretching, out-of-phase
$B_{1g}(5)$	560.9	584		594		597		595		592		593	Fe-O(1) stretching
$B_{2g}(1)$	105.5	103	109.8	109	110.9	111	111.1	109	107.7	109	110.6	109	$R(z)$, in-phase in x-z, out-of-phase in y
$B_{2g}(2)$	143.0	144	157.4	159	159.3	163	159.9	161	160.1	161	162.8	161	$R(x)$, out-of-phase
$B_{2g}(3)$	166.5	172	255.0	278	271.1	291	289.3	299	302.7	305	324.9	311	$[101]_{\text{pc}}$ FeO ₆ rotation, in-phase
$B_{2g}(4)$		329		346		348		349		349		351	O(1) x-z plane
$B_{2g}(5)$	416.8	401	462.8	460	468.2	469	478.9	474	485.6	478	493.7	482	O(1)-Fe-O(2) scissor-like bending
$B_{2g}(6)$		481	521.5	513	524.5	521	531.7	528	535.8	528		534	O(2)-Fe-O(2) scissor-like bending, in-phase
$B_{2g}(7)$	625.1	622	640.5	610	638.1	613	640.5	612		611	624.2	612	Fe-O(2) stretching, in-phase
$B_{3g}(1)$		137	145.0	135	133.6	134	132.2	129		126		123	$R(y)$ out-of-phase in x-z, y
$B_{3g}(2)$	316.8	300	322.8	313		315		312		311		311	O(1)-Fe-O(2) in-phase
$B_{3g}(3)$	436.0	425	432.7	424	429.9	424	431.5	426	433.3	422	433.1	424	octahedra squeezing in y
$B_{3g}(4)$	428.6	408	455.9	447	456.7	452	465.0	455	468.8	457	473.7	460	O(2)-Fe-O(2) scissor-like bending, out-of-phase
$B_{3g}(5)$	641.9	650		641		643		640		637	639.4	637	FeO ₆ breathing

transition from the high-symmetry parent cubic perovskite phase. If a vibrational displacement is directly related to the order parameter, the phonon mode is called soft mode [14, 44] and can experience very large frequency shifts.

Thus our Raman data across the $R\text{FeO}_3$ family exhibits patterns that provide useful insights into the relations among structural order parameters, associated phonon frequencies, and steric effects driven by the R cation. To understand such patterns better, it is useful to think in terms of the simplest Landau-like potential connecting all the relevant ingredients, which we introduce in the following. Let Q denote the relevant structural order parameter, which may correspond to either antiphase or in-phase FeO₆ rotations in the case of orthoferrite perovskites. Also, let η be the isotropic strain of the material, and let us assume that $Q = \eta = 0$ cor-

responds to the ideal cubic perovskite. We can write the Landau free energy as a function of these variables as

$$\Delta F(Q, \eta) = \frac{1}{2}A'(T - T_t)Q^2 + \frac{1}{4}BQ^4 + \frac{1}{2}C\eta^2 + \gamma\eta Q^2, \quad (1)$$

where the $A'(T - T_t)$ and B parameters define the potential well associated to the Q -instability, and we have assumed the simplest temperature (T) dependence of the quadratic term as customarily done in Landau theory. We want to focus on the behavior of the material at temperatures well below the structural transition between the cubic and orthorhombic phases; hence, the transition region is of no interest to us and we can assume a simple fourth-order potential to describe the energy surface, introducing a characteristic $T_t \gg T$ whose precise meaning (i.e., whether or not it coincides with the actual transition temperature) is irrelevant here. Our Landau-like potential also includes an elastic constant C that quantifies the stiffness of the material, as well as the lowest-order

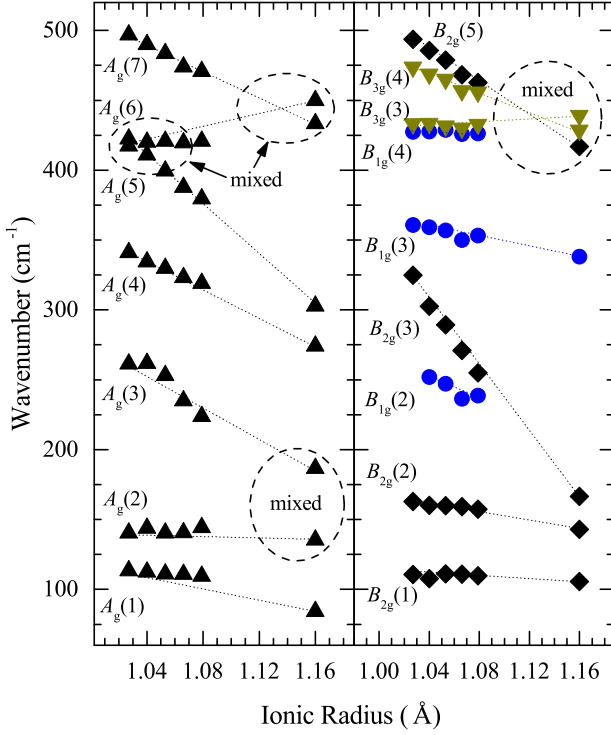


Figure 4: Raman phonon wavenumbers of $R\text{FeO}_3$ as a function of the rare earth R^{3+} ionic radius. All lines are guides to the eye only.

coupling between η and Q that is allowed by symmetry. (Because η is a fully-symmetric strain, the coupling that goes as $\sim \eta Q^2$ always exists irrespective of the symmetry of Q ; further, this is the lowest-order coupling provided that Q is a symmetry-breaking order parameter, as it is the case here.)

In principle, we could write such a potential for each of the orthoferrites, fit the corresponding parameters to reproduce experimental data, etc. However, here we would like to test the following hypothesis: we assume that all the $R\text{FeO}_3$ orthoferrites present the same parameters quantifying the energetics of Q and η , and that the only feature changing from compound to compound is the value of the strain η , as dictated by the size of the rare-earth cation. More specifically, let \bar{r} be a reference value for the ionic radii of the R^{3+} cations (for the sake of concreteness, we can think of \bar{r} as an average value), and let r be the radius of the rare-earth cation for a particular $R\text{FeO}_3$ compound; then, such a compound is characterized by a strain $\eta = \kappa(r - \bar{r})$, where κ is a suitable proportionality constant. We can further consider a Landau potential as the above one, but corresponding to some sort of average orthoferrite (i.e., with parameters obtained as an average of the parameters of specific compounds), substitute the expression for $\eta = \eta(r)$, and postulate the resulting r -dependent potential as applica-

ble to the whole family:

$$\Delta F(Q, r) = \frac{1}{2}[A'(T - T_t) + \kappa\gamma(r - \bar{r})]Q^2 + \frac{1}{4}BQ^4. \quad (2)$$

A key point to realize here is that the compound dependence is restricted to the harmonic part of the potential. Further, formally, the ionic radius r plays the exact same role as the temperature.

Now, let us introduce $\bar{A} = A'(T - T_t) + \kappa\gamma(r - \bar{r})$. Then, it is straightforward to derive

$$Q_{\text{eq}} = \pm(-\bar{A}/B)^{1/2} \quad (3)$$

for the equilibrium order parameter at $T \ll T_t$. (At such a temperature, we assume $\bar{A} < 0$ for all relevant r values.) Further, the associated soft-mode frequency is

$$\omega = \sqrt{\frac{2B}{m}} Q_{\text{eq}}, \quad (4)$$

where m is a mass characteristic of the Q order parameter; for our FeO_6 -rotational cases, this reduces to the mass of the oxygen atom. Now, combining these equations we can write

$$\omega = \sqrt{\frac{2B}{m}} Q_{\text{eq}} = \left[-\frac{A'(T - T_t) + \kappa\gamma(r - \bar{r})}{m/2} \right]^{1/2}, \quad (5)$$

which gives us the desired relation between the compound-dependent parameter (the ionic radius r), temperature, the relevant structural distortion, and its corresponding phonon frequency. In other words, we expect a linear relation between order parameter Q , i.e. the octahedra tilt angle, and the corresponding soft-mode frequency ω , which is solely dependent on the ionic radius r of the rare earth and the temperature T . In particular, if we fix $T = T_{\text{RT}}$, this expression allows us to compare (and predicts the behavior of) the structural and Raman data across the orthoferrite series.

In order to apply this relation to the orthoferrite family, the identification of the soft modes is crucial. An order parameter may give rise to several soft modes which do not necessarily need to be Raman active. However, using the group theoretical formalism of Landau theory, Birman [45] and Shigenari [46] demonstrated that one of the soft modes related to an order parameter has a Raman-active A_g symmetry. In the $Pnma$ structure it is therefore common to focus on the A_g soft modes. From our DFT calculations leading to the assignment of the bands to the respective vibrational pattern (see Table II), we find that $A_g(3)$ and $A_g(5)$ are the soft-modes to corresponding $Q_{[010]_{\text{pc}}}$ and $Q_{[101]_{\text{pc}}}$, respectively, where $Q_{[010]_{\text{pc}}}$ and $Q_{[101]_{\text{pc}}}$ are the order parameters of the $Pnma$ structure representing the octahedra rotations around the $[010]_{\text{pc}}$ (in-phase) and the $[101]_{\text{pc}}$ (antiphase) axes. The assignment of the $A_g(3)$ as a soft-mode is at variance with earlier work by Todorov and co-workers [18] and underlines the importance of precise calculations to gain full understanding of the experimental findings.

Fig. 5 presents the evolution of the soft modes $A_g(3)$ and $A_g(5)$ against the corresponding tilt angle. For completeness and in order to test the general validity of this model, we extend our graph with literature data on orthoferrites with Lu, Tm, Er, Ho and Nd [47–50]. The evolution shows the expected linear relation between the vibrational frequencies and the tilt angles of the $R\text{FeO}_3$. This adds further support to the proposed soft-mode-like relation of tilt frequency and size of the rare earth, not only in the orthoferrites, but also for other families where this behavior has been experimentally verified: orthomanganites [15], orthochromates [17], orthoscatates [16] among others [18]. However, at variance with these previous experimental data, our work on orthoferrites show two additional features that have to be commented on, namely that i) the two tilt modes follow two different lines and ii) LaFeO_3 deviates significantly from the general linear behaviour.

The octahedral-rotation angles and soft-mode frequencies do not present the same scaling for the different order parameters. The rotation $Q_{[010]_{\text{pc}}}$ about $[010]_{\text{pc}}$ reveals a scaling factor of $21.1 \text{ cm}^{-1}/\text{deg}$ whereas the slope of the rotation $Q_{[101]_{\text{pc}}}$ about $[101]_{\text{pc}}$ gives $23.9 \text{ cm}^{-1}/\text{deg}$. This is natural and expected when bearing in mind that the two soft modes are associated to two independent order-parameters. The relation in Eq. 5 needs to be separately considered for each of the relevant order parameters (in-phase and antiphase FeO_6 rotations in our case), and there is no reason to expect that the values of the coefficients in our Landau potential will be the same for different cases. However, this difference was never pointed out in previous investigations [15–18]. This probably comes from a combination of factors including experimental difficulties in mode assignment and frequency determination, scattered data from a more limited number of compounds, and possibly differences in scaling factors coincidentally too small to be resolved experimentally. We believe that a careful (re)investigation of the other series will reveal this difference.

Last, we investigate the case of LaFeO_3 in more details. For LaFeO_3 , no A_g Raman mode actually follows the scaling given by the other members of the series. Instead, the $A_g(2)$ and $A_g(3)$ modes, plotted as open triangles in Fig. 5, fall below and above the scaling line respectively. On the other hand, we have already pointed out that the band positions in LaFeO_3 differ significantly from the other orthoferrites and do not seem to follow from a continuous evolution of the other spectra. In order to rationalize this comparatively exotic behaviour, we analyzed in details the vibrational patterns given from our first-principles calculations for LaFeO_3 and SmFeO_3 . This comparison reveals several frequency ranges where the modes do not keep their atomic displacement patterns from La to Sm, but instead exhibit mixed characteristics, which is expected from mode coupling phenomena between two modes of the same symmetry getting close to each other. In LaFeO_3 , the mode mixing occurs in the regions between 100 and 200 cm^{-1} and 400 and 450 cm^{-1}

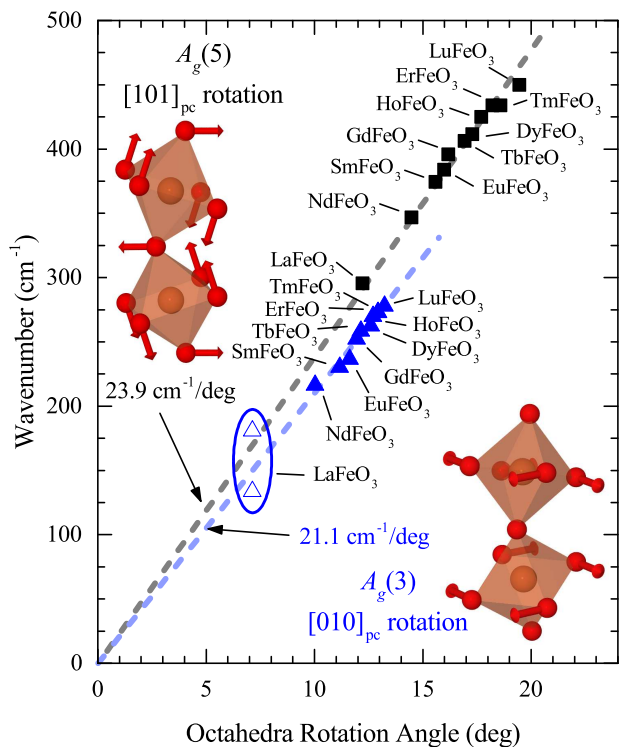


Figure 5: $R\text{FeO}_3$ soft-mode wavenumbers at ambient conditions as a function of octahedra-tilt angles for the $A_g(3)$ and $A_g(5)$ modes. Data from this work are complemented by literature data for NdFeO_3 [50]), HoFeO_3 and TmFeO_3 [48], ErFeO_3 [49]) and LuFeO_3 [47]. The oval and the open symbols point out the mode mixing region of the $A_g(2)$ and $A_g(3)$ modes for LaFeO_3 , as discussed in the text.

as indicated in Fig. 4. In particular, it strongly affects the lower soft mode $A_g(3)$ as it approaches the lower lying $A_g(2)$. For Sm^{3+} and smaller cations, these two modes have very distinguishable atomic displacement patterns, with the $A_g(2)$ mode being dominated by R^{3+} displacements while $A_g(3)$ is dominated by octahedral rotations. In contrast, in LaFeO_3 , the two modes have significant contributions from both La^{3+} displacement and octahedral rotations. It is therefore no longer possible to identify any of them as the soft mode of interest associated to octahedral tilts only. The soft-mode frequency for a hypothetical unmixed-state would lie between the two positions. This in turns enable us to understand why the Raman spectrum LaFeO_3 is significantly different as a whole from the others members of the series, since the mode coupling will affect band positions and intensities. This behavior par excellence has been reported by Iliev et al. in orthomanganites [51], was also found in the $(\text{La},\text{Sm})\text{CrO}_3$ solid solutions [41] and is probably a general phenomenon occurring in orthorhombic $Pnma$ perovskites in the limit of small tilt angles, where distortions of the octahedra have to be taken into account [52].

IV. CONCLUSION

We have presented a Raman scattering study of a series of orthoferrites $R\text{FeO}_3$ ($R = \text{La}, \text{Sm}, \text{Eu}, \text{Gd}, \text{Tb}, \text{Dy}$). A symmetry assignment of the observed modes has been presented on the basis of a single-crystal study of SmFeO_3 and DFT calculations, and by taking advantage of the continuous changes in the Raman spectra across the whole $R\text{FeO}_3$ series. This careful assignment has allowed to relate most of the vibration modes to their vibrational pattern and symmetries. Based on this, we can follow the structural evolution across the series and we have namely shown that the $A_g(3)$ and $A_g(5)$ modes are the soft-modes of A_g symmetry which correspond to the octahedral-rotation order-parameters $Q_{[010]_{\text{pc}}}$ (in-phase octahedral tilts about the $[010]$ pseudocubic axis) and $Q_{[101]_{\text{pc}}}$ (antiphase octahedral tilts about pseudocubic $[101]$). In this framework we have demonstrated the proportionality of soft-mode frequency and order parameter. Furthermore we have shown that for rare-earth orthoferrites (and similar series) the change of the soft-mode frequency depends only on the size of the rare earth (for a fixed temperature). This work provides reference data for structural investigation of the orthoferrite $R\text{FeO}_3$ fam-

ily, and will be helpful in further studies of phenomena in orthoferrites including structural instabilities, possible ferroelectricity and multiferroicity, and rare-earth magnetism at low temperature via spin-phonon coupling.

Acknowledgments

The authors thank R. Haumont (Université Paris Sud), B. Dkhil (Université Paris Saclay) and W. Ren (Shanghai University), E. Queiros and P.B. Tavares (University of Trás-os-Montes e Alto Douro), and M. Mihalik jr., M. Mihalik, and M. Zentkova (Slovak Academy of Sciences) for providing high-quality samples. MCW, MG, HJZ, JI and JK acknowledge financial support from the Fond National de Recherche Luxembourg through a PEARL grant (FNR/P12/4853155/Kreisel). JMA and AA acknowledge for financial support through projects Norte-070124-FEDER-000070, UID/NAN/50024/2013, PTDC/FIS-NAN/0533/2012 and VEGA2/0132/16. RV thanks for financial support through the grant PD/B1/106014/2015 by FCT.

-
- [1] R. L. White, Journal of Applied Physics **40**, 1061 (1969).
 - [2] R. M. White, R. J. Nemanich, and C. Herring, Physical Review B **25**, 1822 (1982).
 - [3] M. Eibschütz, S. Shtrikman, and D. Treves, Physical Review **156**, 562 (1967).
 - [4] H. J. Zhao, J. Íñiguez, X. M. Chen, and L. Bellaiche, Physical Review B **93**, 014417 (2016).
 - [5] S. Cao, H. Zhao, B. Kang, J. Zhang, and W. Ren, Scientific reports **4**, 5960 (2014).
 - [6] L. G. Marshall, J.-G. Cheng, J.-S. Zhou, J. B. Goodenough, J.-Q. Yan, and D. G. Mandrus, Physical Review B **86**, 064417 (2012).
 - [7] Y. Tokunaga, N. Furukawa, H. Sakai, Y. Taguchi, T.-h. Arima, and Y. Tokura, Nature materials **8**, 558 (2009).
 - [8] Y. Du, Z. X. Cheng, X. L. Wang, and S. X. Dou, Journal of Applied Physics **107**, 09D908 (2010).
 - [9] J.-H. Lee, Y. K. Jeong, J. H. Park, M.-A. Oak, H. M. Jang, J. Y. Son, and J. F. Scott, Physical Review Letters **107**, 117201 (2011).
 - [10] C.-Y. Kuo, Y. Drees, M. T. Fernández-Díaz, L. Zhao, L. Vasylechko, D. Sheptyakov, A. M. T. Bell, T. W. Pi, H.-J. Lin, M.-K. Wu, E. Pellegrin, S. M. Valvidares, Z. W. Li, P. Adler, A. Todorova, R. Küchler, A. Steppke, L. H. Tjeng, Z. Hu, and A. C. Komarek, Physical Review Letters **113**, 217203 (2014).
 - [11] Z. Cheng, F. Hong, Y. Wang, K. Ozawa, H. Fujii, H. Kimura, Y. Du, X. Wang, and S. Dou, ACS Applied Materials and Interfaces (2014).
 - [12] P. Fleury, J. Scott, and J. Worlock, Physical Review Letters **21**, 16 (1968).
 - [13] J. Scott, R. Leite, and T. Damen, Physical Review **188**, 1285 (1969).
 - [14] J. F. Scott, Reviews of Modern Physics **46**, 83 (1974).
 - [15] M. Iliev, M. Abrashev, J. Laverdière, S. Jandl, M. Gospodinov, Y.-Q. Wang, and Y.-Y. Sun, Physical Review B **73**, 3 (2006).
 - [16] O. Chaix-Pluchery and J. Kreisel, Phase Transitions **84**, 542 (2011).
 - [17] M. C. Weber, J. Kreisel, P. A. Thomas, M. Newton, K. Sardar, and R. Walton, Physical Review B **85**, 054303 (2012).
 - [18] N. D. Todorov, M. V. Abrashev, and V. G. Ivanov, Journal of physics. Condensed matter : an Institute of Physics journal **24**, 175404 (2012).
 - [19] J. Laverdière, S. Jandl, A. Mukhin, V. Ivanov, and M. Iliev, Physical Review B **73**, 214301 (2006).
 - [20] W. S. Ferreira, J. Agostinho Moreira, A. Almeida, M. R. Chaves, J. P. Araújo, J. B. Oliveira, J. M. Machado Da Silva, M. A. Sá, T. M. Mendonça, P. Simeão Carvalho, J. Kreisel, J. L. Ribeiro, L. G. Vieira, P. B. Tavares, and S. Mendonça, Physical Review B **79**, 054303 (2009).
 - [21] J. A. Moreira, A. Almeida, W. S. Ferreira, J. E. Araújo, A. M. Pereira, M. R. Chaves, J. Kreisel, S. M. F. Vilela, and P. B. Tavares, Physical Review B **81**, 054447 (2010).
 - [22] V. S. Bhadram, B. Rajeswaran, A. Sundaresan, and C. Narayana, EPL (Europhysics Letters) **101**, 17008 (2013).
 - [23] M. El Amrani, M. Zaghrioui, V. Ta Phuoc, F. Gervais, and N. E. Massa, Journal of Magnetism and Magnetic Materials **361**, 1 (2014).
 - [24] D. A. Tenne, A. Bruchhausen, N. D. Lanzillotti-Kimura, A. Fainstein, R. S. Katiyar, A. Cantarero, A. Soukiassian, V. Vaithyanathan, J. H. Haeni, W. Tian, D. G. Schlom, K. J. Choi, D. M. Kim, C. B. Eom, H. P. Sun, X. Q. Pan, Y. L. Li, L. Q. Chen, Q. X. Jia, S. M. Nakhmanson, K. M. Rabe, and X. X. Xi, Science (New York, N.Y.) **313**, 1614

- (2006).
- [25] M. C. Weber, M. Guennou, N. Dix, D. Pesquera, F. Sánchez, G. Herranz, J. Fontcuberta, L. López-Conesa, S. Estradé, F. Peiró, J. Iñiguez, and J. Kreisel, **3**, 1 (2016).
 - [26] J. Kreisel, M. C. Weber, N. Dix, F. Sánchez, P. A. Thomas, and J. Fontcuberta, *Advanced Functional Materials* **22**, 5044 (2012).
 - [27] J. A. Moreira, A. Almeida, W. S. Ferreira, M. R. Chaves, J. B. Oliveira, J. M. M. da Silva, M. A. Sá, S. M. F. Vilela, and P. B. Tavares, *Journal of Electroceramics* **25**, 203 (2010).
 - [28] J. P. Perdew, A. Ruzsinszky, G. I. Csonka, O. A. Vydrov, G. E. Scuseria, L. A. Constantin, X. Zhou, and K. Burke, *Physical Review Letters* **100**, 136406 (2008).
 - [29] G. Kresse and J. Furthmüller, *Physical Review B* **54**, 11169 (1996).
 - [30] G. Kresse and D. Joubert, *Physical Review B* **59**, 1758 (1999).
 - [31] S. L. Dudarev, G. A. Botton, S. Y. Savrasov, C. J. Humphreys, and a. P. Sutton, *Physical Review B* **57**, 1505 (1998).
 - [32] P. E. Blöchl, *Physical Review B* **50**, 17953 (1994).
 - [33] A. M. Glazer, *Acta Crystallographica Section B Structural Crystallography and Crystal Chemistry* **28**, 3384 (1972).
 - [34] R. H. Mitchell, *Perovskites: Modern and ancient*, Almaz Press, Ontario, 2002.
 - [35] H. D. Megaw, *Crystal structures: A working approach*, W.B. Saunders Co., Philadelphia PA, 1973.
 - [36] Y. Zhao, D. J. Weidner, J. B. Parise, and D. E. Cox, *Physics of the Earth and Planetary Interiors* **76**, 17 (1993).
 - [37] R. D. Shannon, *Acta Crystallographica A* **32** (1976).
 - [38] M. Marezio, J. P. Remeika, and P. D. Dernier, *Acta Crystallographica Section B Structural Crystallography and Crystal Chemistry* **26**, 2008 (1970).
 - [39] M. Marezio and P. Dernier, *Materials Research Bulletin* **6**, 23 (1971).
 - [40] E. Kroumova, M. Aroyo, J. Perez-Mato, A. Kirov, C. Capillas, S. Ivantchev, and H. Wondratschek, *Phase Transitions* **76**, 155 (2003).
 - [41] L. M. Daniels, M. C. Weber, M. R. Lees, M. Guennou, R. J. Kashtiban, J. Sloan, J. Kreisel, and R. I. Walton, *Inorganic chemistry* **52**, 12161 (2013).
 - [42] T. Damen, S. Porto, and B. Tell, *Physical Review* **142**, 570 (1966).
 - [43] M. Iliev, A. Litvinchuk, V. Hadjiev, Y.-Q. Wang, J. Cmaidalka, R.-L. Meng, Y.-Y. Sun, N. Kolev, and M. Abrashev, *Physical Review B* **74**, 214301 (2006).
 - [44] W. Hayes and R. Loudon, *Scattering of Light by Crystals*, John Wiley & Sons, New York, 1978.
 - [45] J. Birman, *Physics Letters A* **45**, 196 (1973).
 - [46] T. Shigenari, *Physics Letters A* **46**, 243 (1973).
 - [47] S. Venugopalan and M. M. Becker, *The Journal of Chemical Physics* **93**, 3833 (1990).
 - [48] S. Venugopalan, M. Dutta, A. K. Ramdas, and J. P. Remeika, *Physical Review B* **31**, 1490 (1985).
 - [49] N. Koshizuka and S. Ushioda, *Physical Review B* **22**, 5394 (1980).
 - [50] M. K. Singh, H. M. Jang, H. C. Gupta, and R. S. Katiyar, *Journal of Raman Spectroscopy* **39**, 842 (2008).
 - [51] M. N. Iliev, M. V. Abrashev, J. Laverdière, S. Jandl, M. M. Gospodinov, Y.-Q. Wang, and Y.-Y. Sun, *Physical Review B* **73**, 064302 (2006).
 - [52] J.-S. Zhou and J. B. Goodenough, *Physical Review Letters* **94**, 065501 (2005).